Applied Surface Science 661 (2024) 160086

Contents lists available at ScienceDirect

Applied Surface Science

journal homepage: www.elsevier.com/locate/apsusc

Full Length Article

# Sol-gel synthesis of tetragonal $BaTiO_3$ thin films under fast heating

Yang Liu [a], Sirui Li [a], Fausto Gallucci [a], Evgeny V. Rebrov [a,b,*]

[a] Department of Chemical Engineering and Chemistry, Eindhoven University of Technology, Eindhoven 5612 AP, the Netherlands
[b] School of Engineering, University of Warwick, Coventry CV4 7AL, United Kingdom

ARTICLE INFO

*Keywords:*
Tetragonal $BaTiO_3$ films
Inductive heating
Sol–gel

ABSTRACT

$BaTiO_3$ thin films with a thickness of 400 nm were prepared by spin coating onto a quartz plate and subsequently calcined at 700 °C. The effect of fast (540 K $min^{-1}$) and slow (10 K $min^{-1}$) heating on morphology, unit cell parameter and dielectric constant was studied. Fast heating yields tetragonal $BaTiO_3$ films with a semiconductor band gap of 3.54 eV, dielectric constant of 685 and a surface roughness of 12 nm. In contrast, slow heating produces tetragonal $BaTiO_3$ films with a larger band gap of 3.78 eV, a dielectric constant of 219 and a surface roughness of 35 nm. A kinetic constant of 0.0061 $min^{-1}$ was obtained in the decomposition of methylene blue with UV light over BTO films at 20 °C.

## 1. Introduction

Perovskite materials are the most widely used ferroelectric materials in the industry and have been the subject of recent studies [1]. Among them, barium titanate ($BaTiO_3$, BTO) is the most widely used ferroelectric material, and even eighty years after its discovery, it remains the most important ceramic dielectric applied among others in power electronics, biomedical applications, and non-thermal plasma reactors [2–4]. A BTO-based capacitor is considered as one of the candidates for pulsed power systems due to its high permittivity. BTO films with high dielectric constant and low loss have attracted significant attention as capacitors in power electronics [2,5]. Recently there has been interest in plasma-assisted $CO_2$ utilization using various non-thermal plasma processes. Xu et al. employed BTO in non-thermal plasma reactors to enhance electric field which in turn resulted in an increase of $CO_2$ conversion [6]. A packed bed reactor with a BTO ferroelectric packing provided a considerably higher conversion in $CO_2$ decomposition and also higher energy efficiency than a reactor without packed materials. In plasma, ionized gas particles exist in a highly energized state, resulting in the presence of free electrons and positive ions which can interact with electromagnetic field. The local electrical field for a given voltage increases proportinally to the dielectric constant of ferroelectric films deposed onto the electrodes [7]. Therefore obtaining materials with high dielectric constant is an attractive strategy to increase the reactant conversion in plasma reactors. Beyond applications in plasma assisted reactions, the BTO films were applied as an efficient photocatalyst. Tetragonal BTO showed a higher photocatalytic activity in methylene blue decomposition than cubic BTO [8]. Oxygen vacancies in the BTO surface enhance the internal electric field and improve the photocatalytic ammonia production under a magnetic field [9]. There is a strong correlation between the particle size and the dielectric properties of BTO. The particle size of BTO depends on the synthesis method [10]. Different synthetic approaches were applied to obtain nano-structured BTO, both in the form of powders and thin films: viz hydrothermal and solvothermal synthesis, co-precipitation, and sol–gel methods [11–14]. In the sol–gel method, the precursor sol is first prepared and then followed by depositing the sol on the substrate via methods such as spin coating and dip coating. And a subsequent calcination process is generally needed to obtain crystallized thin films after coating.

Conventional calcination at rather slow heating rates often leads to a lengthy calcination process. Therefore, there is a need to intensify the process to produce nanosized BTO films in a shorter time. Fast heating in microwaves was already demonstrated for lead-free ferroelectric $CaBi_4Ti_4O_{15}$ ceramics and the calcination step was completed in 20 min [15]. In the synthesis of $LaCoO_3$ nanoparticles, the duration of calcination was further reduced to 10 min [16]. BTO films onto a Si substrate were calcined under microwave heating for 2.5 min [17]. A highly ordered BTO nanowires with a length of 900 nm and a width of 20–100 nm were obtained.

Rapid thermal annealing (RTA) was also used to reduce the annealing time [18]. Imhoff et al. applied RTA to calcine Pb ($Fe_{0.5}Nb_{0.5}$)$O_3$ thin films at 650 °C for just 1 min with a heating rate of 50 K $s^{-1}$ [19]. A tube furnace at around 1300 °C was used to achieve the fast-sintering for BTO powders with a heating rate of around 200 K $min^{-1}$ followed by

* Corresponding author at: Department of Chemical Engineering and Chemistry, Eindhoven University of Technology, Eindhoven 5612 AP, the Netherlands.
*E-mail addresses:* e.rebrov@tue.nl, e.rebrov@warwick.ac.uk (E.V. Rebrov).

https://doi.org/10.1016/j.apsusc.2024.160086
Received 4 December 2023; Received in revised form 31 March 2024; Accepted 10 April 2024
Available online 11 April 2024

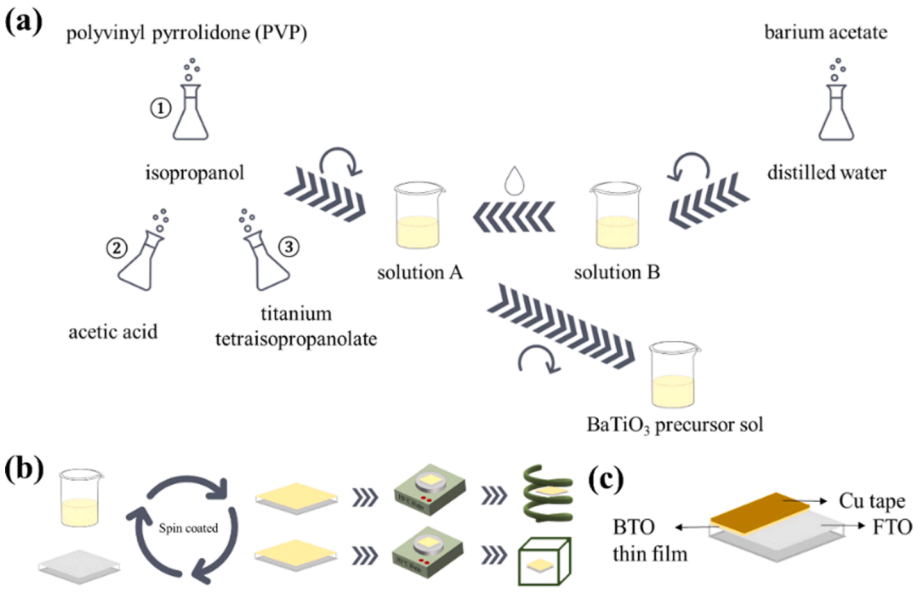


**Fig. 1.** Schematic view of preparation method for the BTO films onto a quartz substrate. (a) Making precursor solution; (b) spin coating steps followed by calcination; (c) assembly of a composite film for dielectric constant measurements.

a dwell interval of 5–15 min [20].

It can be concluded that fast heating rates during calcination step led to nanostructured films within a shorter time. While microwave heating is clearly an enabling technology, it still has several drawbacks. Electrically conductive substrates cannot be used in microwaves and many unconducive substates have also rather low thermal conductivity which limits the heating rate to avoid large thermal gradients. Also scaling up of microwave heating to larger substrates is not straightforward as the exact distribution of electric field inside the microwave is difficult to predict. This again may lead to non-uniform substrate heating which creates inhomogeneities inside the films obtained. Inductive heating operates at frequencies in the kHz range, that provide a uniform electromagnetic (EM) field across the substrate. Also conductive substrates can be used under inductive heating which simplifies deposition of thin films onto them. Nonconductive substrate can be used as well, however they require a susceptor of the EM irradiation (such as a metal plate) to be placed in close contact for the best performance.

Therefore, the goal of this work was to explore the effect of fast heating mode in the preparation of BTO films. In fast heating, the objective is to enhance the ratio of densification rate to coarsening rate. Because coarsening mechanisms, such as lattice and grain-boundary diffusion, commonly dominate over densification mechanisms, such as surface diffusion, at lower temperatures, it has been suggested that rapid heating can be beneficial to achieve high density coupled with fine grain size and fast crystallization. The films obtained under fast heating were compared with those obtained under conventional (slow) heating.

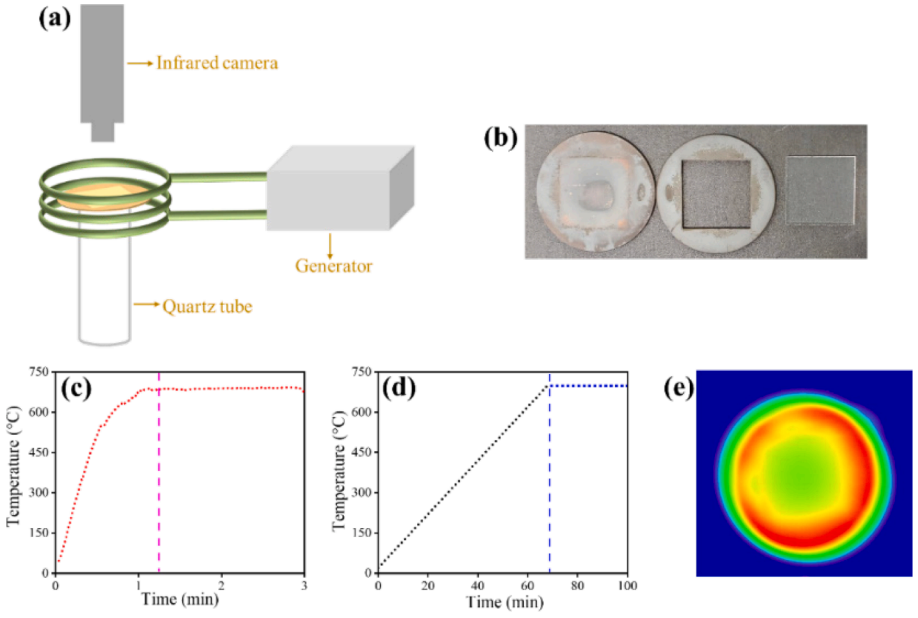


**Fig. 2.** (a) Schematic view of the inductive heating set-up; (b) optical image of the two stainless steel susceptor plates and the 20 mm × 20 mm quartz substrate; (c) mean substrate temperature as a function of time; (d) mean substrate temperature as a function of time under conventional heating in a convective oven; (e) temperature distribution map under inductive heating. A temperature gradient (the difference between the green and yellow colors of 10 K is observed). (For interpretation of the references to colour in this figure legend, the reader is referred to the web version of this article.)

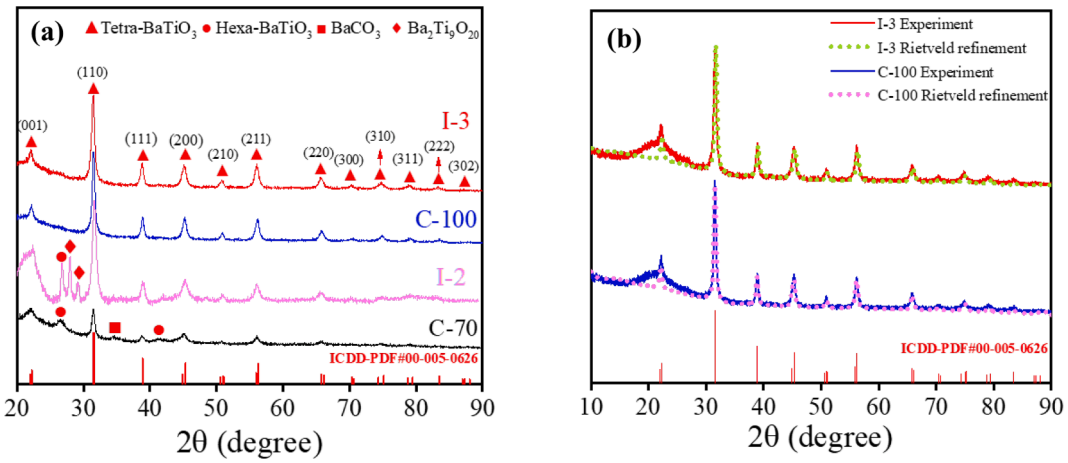


**Fig. 3.** (a) XRD patterns of I-2, I-3, C-100 and C-70 samples; (b) XRD Rietveld refinement of I-3 and C-100 samples.

## 2. Experimental

### 2.1. Preparation of thin films

Fig. 1(a) shows the preparation process of the BTO precursor solution adopted from [21]. Barium acetate and titanium isopropoxide (99.5 wt %, both from Sigma-Aldrich) were used as Ba and Ti sources, respectively. Solution A was prepared by dissolving 0.06 g polyvinyl pyrrolidone (PVP, Mw = 40000), 2.92 g titanium isopropoxide and 4.54 g acetic acid in 12 g isopropanol (all chemicals from Sigma-Aldrich). Solution B was prepared by dissolving barium acetate (2.56 g) in distilled water (3.6 g). Both solutions were stirred 1 h. Then Solution B was dropwise added into solution A and the resulting precursor solution was stirred for 1 h.

The precursor solution was spin coated onto a quartz plate (20 mm × 20 mm × 1 mm) at 3000 rpm for 30 s following the approach described in [22]. Then the quartz plate was immediately transferred to a hot plate (150 °C) and heated for 10 min to remove the residual solvents. Afterwards, the quartz plate was heated to 700 °C using inductive heating or conventional heating, respectively. For inductive heating, the quartz plate was sandwiched between two stainless-steel plates. The top plate featured an opening of 20 mm × 20 mm to accommodate the quartz plate to ensure more uniform heating (Fig. 2). The inductive heating was performed with a 3-turn coil connected to a 1 kW generator operated at 350 kHz (EasyHeat). The electric current in the coil was adjusted to provide a constant heating rate of 540 K $min^{-1}$ followed by a dwell time of 100 s at 700 °C to get a total processing time of 3 min. The temperature was measured by an IR-camera (FLIR A655) connected to a temperature controller via the Labview software. The control loop allowed to realize a linear heating rate towards the set-point. The IR camera was also used to monitor the formation of any localized hotspots during the heating. Conventional heating was performed in an oven at a heating rate of 10 K $min^{-1}$ followed by a dwell time of 2 or 32 min to get a total processing time of 70 or 100 min.

For the dielectric constant measurements, the precursor solution was spin coated onto one section (20 mm × 10 mm) of a 20 mm × 20 mm × 2 mm fluorine doped tin oxide (FTO) coated glass. The other section of the FTO glass (20 mm × 10 mm) was protected by Teflon tape to make connection to the bottom electrode. A thin copper tape with a size of 20 mm × 10 mm was used as the top electrode (Fig. 1(c)).

### 2.2. Characterization

X-ray diffraction (XRD) was used to detect the crystal structure of the samples on an X-ray diffractometer (Bruker D8) operated at 20 kV and 20 mA, using Cu Kα (λ = 1.5406 Å) radiation in the range from 10 to 90° 2-thetas at a scanning rate of 0.12° $min^{-1}$. The experimental data were refined by Rietveld method which uses the least-squares minimization technique. The operating voltage was 20 kV and the current was 20 mA. The crystallinity was calculated by dividing the area of the peak in the 30–33 degree 2-theta range by the area of this peak in the fully crystalline reference sample. The crystallite size was calculated from the (1 1 0) reflection using the Scherrer equation with a shape factor constant K of 0.9. The lattice parameters $a$ and $c$ were calculated using (1 0 0), (2 0 0) and (0 0 1) reflections, respectively: $a = \lambda \frac{h}{\sin\theta}$, $c = \lambda \frac{l}{\sin\theta}$, and the tetragonality is taken as the $c/a$ ratio. Raman spectra were recorded using a 532 nm laser coupled with a confocal Raman microscope (WITec WMT 50). FTIR spectra were recorded with a FT-IR spectrometer (Nicolet iS50). Prior to the measurements, the films were mechanically removed from the substrate. All FTIR spectra were background corrected. UV–Vis spectra were recorded with a UV–Vis spectrophotometer (Shimadzu UV-2501 PC) in the range from 250 to 700 nm. The semiconductor band gap was calculated by the Tauc plot method. The morphology of the samples was studied by scanning electron microscopy (SEM) on a field emission scanning electron microscope (FESEM, JSM 7001-F, JEOL). The surface roughness was determined with Atomic Force Microscopy (AFM, Asylum Research MFP-3D Origin).

The dielectric permittivity ($\varepsilon = \varepsilon' - i\varepsilon''$) was calculated from the real and imaginary parts of the impedance of the FTO/BTO/Cu assembly ($Z'$ and $Z''$, Eqs. (1) and (2)), which was measured with a potentiostat (BioLogic VMP-300).

$$\varepsilon' = \frac{dZ''}{A\omega\varepsilon_0\left[(Z')^2 + (Z'')^2\right]} \quad (1)$$

$$\varepsilon'' = \frac{dZ'}{A\omega\varepsilon_0\left[(Z')^2 + (Z'')^2\right]} \quad (2)$$

where, $A$ is the film area, $d$ is the film thickness, $\varepsilon_0$ is the permittivity of the free space (8.85 × $10^{-12}$ F $m^{-1}$) and $\omega = 2\pi f$ is the angular frequency [23–25].

### 2.3. Photocatalytic activity test

The photocatalytic decomposition of methylene blue (MB) over BTO thin film obtained under fast heating was studied as a test reaction. A MB aqueous solution (15 mg/L, Sigma-Aldrich) was placed in a quartz reactor. After the initial adsorption in the dark for 30 min, the substate was illuminated with a 270 nm LED light. The size of the light source was considerably larger than the illuminated reactor area, providing a rather uniform intensity throughout the reactor length. The intensity of the absorption band of MB at the 664 nm was measured with UV–Vis

**Table 1**
Crystallinity, crystallite size, lattice parameter and tetragonality of synthesized BTO films.

| Sample code | Crystallinity (%) | Crystallite Size (nm) | Lattice Parameter a, b, c (Å) | Tetragonality (–) |
|---|---|---|---|---|
| Reference | 100 | 14.0 | 3.992, 3.992, 4.030 | 1.010 |
| I-3 | 98 | 12.9 | 4.008, 4.008, 4.080 | 1.018 |
| C-100 | 86 | 13.9 | 3.998, 3.998, 4.020 | 1.005 |
| C-70 | 40 | M | – | – |

M = mixture of several phases.

spectroscopy. Blank experiments were also carried out with an empty quartz substrate to obtain the rate of non-catalytic decomposition under the same experimental conditions.

## 3. Results and discussion

### 3.1. Phase composition

A total processing time of 3 min was the minimum to obtain fully crystalline films under fast heating (sample I-3, Fig. 3(a)). Fully crystalline films cannot be obtained at shorter processing times. The XRD pattern of I-2 shows a partially amorphous material. However, the XRD pattern of I-3 agrees well with the standard XRD pattern of tetragonal BTO (05-0626 JCPDF data file). The films are characterized by well-resolved diffraction peaks at 22.26, 31.49, 38.88, 45.38, 51.10, 56.10, 65.75, 70.66, 74.33, 79.47, 83.49 and 87.28° 2-theta, corresponding to (0 0 1), (1 1 0), (1 1 1), (2 0 0), (2 1 0), (2 1 1), (2 2 0), (3 0 0), (3 1 0), (3 1 1), (2 2 2) and (3 0 2) planes of tetragonal BTO [26,27]. The second peak observed at 2-theta of 31.49° matches the highest intensity peak of the BTO, which corresponds to the (1 1 0) plane of the perovskite structure, confirming that the crystallites are preferably orientated along (1 1 0) plane. Analysis of the preferred orientations indicates that the relative intensities of the diffraction peaks are in agreement with those obtained from BTO standards, proving that the substrate has not induced preferential directions in the film growth. Much longer times were required at conventional heating. The XRD patterns of film samples calcined under slow heating after 70 and 100 min (C-70 and C-100, respectively) are also shown in Fig. 3(a). It can be seen that the C-70 sample is a mixture of BTO and $BaCO_3$ with a rather low crystallinity. A pure tetragonal BTO phase was also obtained under slow heating only after 100 min. The crystallinity, mean crystallite size, lattice parameters and tetragonality of the film samples are listed in Table 1. The mean crystallite size of BTO films remains essentially the same under fast and slow heating. However, both crystallinity and tetragonality were improved under fast heating. Therefore, it can be inferred that fast heating accelerates the kinetics of BTO formation during the calcination step and also facilitates to obtain the tetragonal BTO.

Fu et al. [17] assumed that motions of atoms (lattice diffusion) due to direct volumetric heating results in a fast crystallization. Zhu et al. [20] concluded that lattice diffusion is accompanied by densification while the grain growth (e.g., surface diffusion) is suppressed. Zhang et al. [28] reported that fast heating enhances the ion diffusion during crystallization of $PbTiO_3$ (PTO) which induces the formation of stable crystal nucleus and reduces the crystal size. In addition, fast heating reduced the effective activation energy for the nucleation and grain growth of the perovskite phase by 39%. Thus fast heating can reduce the nucleation time and produce a large number of smaller crystals as compared to slow heating.

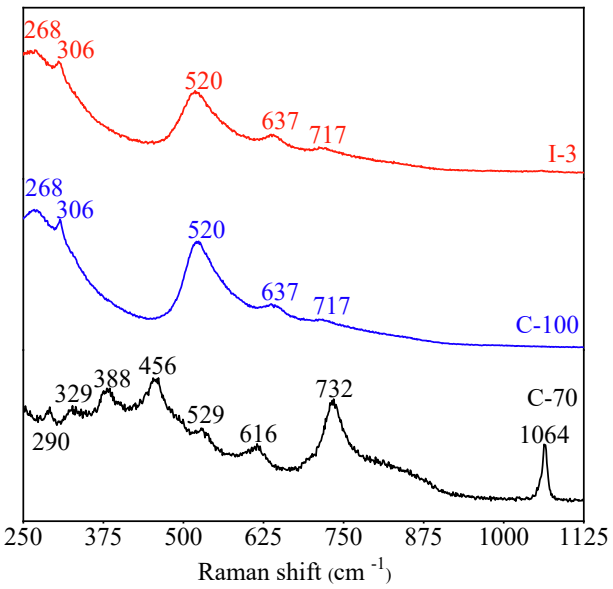


**Fig. 4.** Raman spectra of I-3, C-70 and C-100 samples.

**Table 2**
Raman modes of I-3 and C-100 vs literature data.

| Mode | DiDomenico et al. [33] | Pinczuk et al. [34] | This work |
|---|---|---|---|
| $A_1(TO_2)$ | 267 | 270 | 268 |
| $E(TO_3 + LO_2) + B_1$ | 308 | 305 | 306 |
| $A_1(LO_2)$ | 473 | 471 | – |
| $A_1(TO_3) + E\ (TO_4)$ | 512 | 516 | 520 |
| $A_1(LO_3) + E\ (LO_4)$ | 740 | 719 | 717 |

### 3.2. Raman and IR spectra

Raman spectroscopy was used to characterize the structure of the prepared films (Fig. 4). It should be mentioned that cubic BTO (Pm3m) demonstrates no Raman activity. For tetragonal BTO (P4mm), eight Raman active modes are predicted, including four modes of E symmetry, three modes of A1 symmetry and a single mode of B1 symmetry [29]. In addition, each of these eight Raman modes splits into longitudinal (LO) and transverse (TO) optical reflections because of long-range electrostatic forces induced by the ionicity of the lattice [30]. The I-3 and C-100 samples demonstrate a characteristic pattern of tetragonal BTO [8,31,32]. The assignment of the corresponding modes is listed in Table 2. A broad Raman reflection at 268 $cm^{-1}$ is attributed to the $A_1$ ($TO_2$) mode. A sharp reflection at around 306 $cm^{-1}$ is assigned to $B_1 + E$ ($LO_2$) + E ($TO_3$). An asymmetric broad reflection at 520 $cm^{-1}$ is associated with $A_1$ ($TO_3$) + E ($TO_4$), and a weak broad reflection at 717 $cm^{-1}$ is assigned to a sum of $A_1$ ($LO_3$) and E ($LO_4$) modes. These modes are typical peaks of tetragonal BTO in the Raman spectrum. It can be concluded that the Raman data are in good agreement with the XRD data and the reported literature data.

In addition, there is a band at 637 $cm^{-1}$ in the spectra of samples I-3 and C-100, typically attributed to hexagonal BTO. Raman spectroscopy is a more sensitive method of detecting minor amounts of impurities (below 1 wt%) which may not be seen in XRD. In the Raman spectrum of

**Table 3**
Raman peak positions of $BaTiO_3$ and $BaCO_3$.

| Phase | Band position ($cm^{-1}$) | References |
|---|---|---|
| Tetragonal $BaTiO_3$ | 268, 306, 520, 717 | [8,32] |
| Hexagonal $BaTiO_3$ | 637 | [32] |
| $BaCO_3$ | 1064 | [35] |

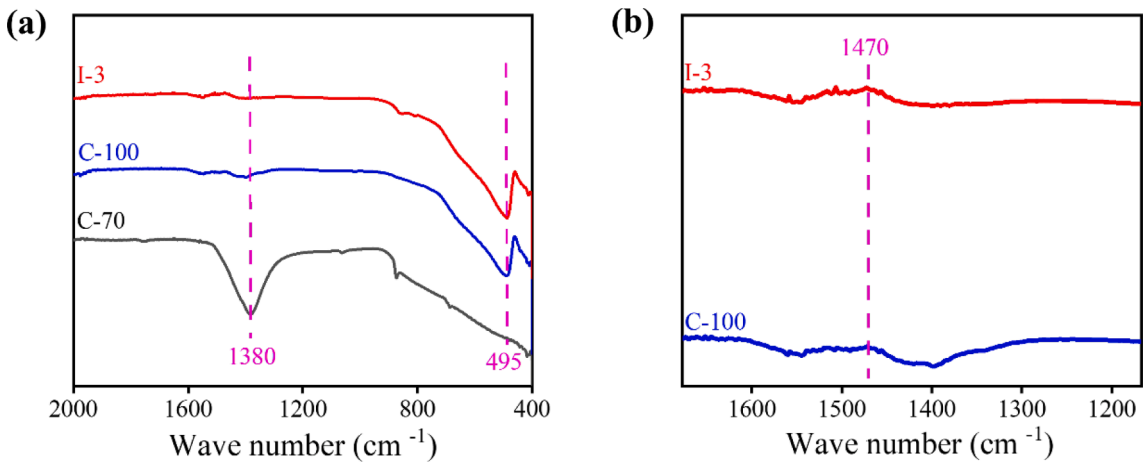


**Fig. 5.** (a) FTIR spectra of I-3, C-70 and C-100 samples; (b) higher resolution spectra of I-3 and C-100 samples in the mid-IR region.

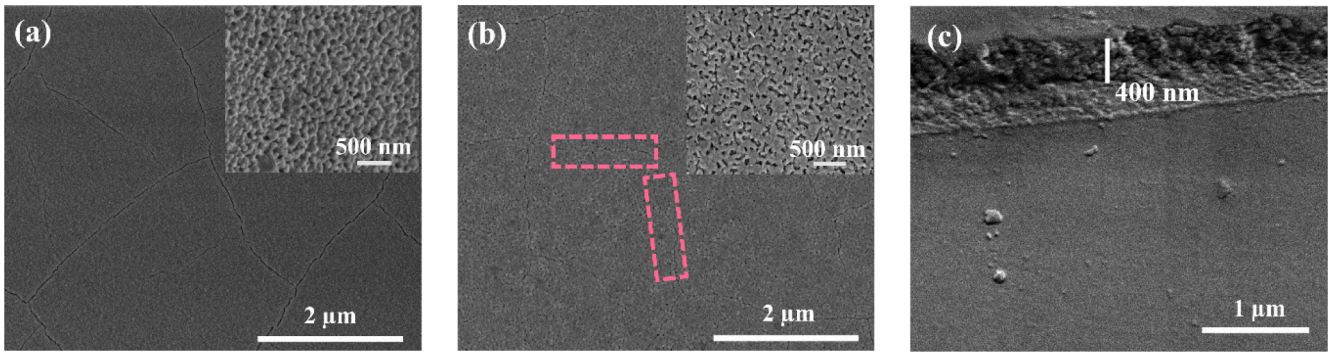


**Fig. 6.** FE-SEM micrographs of (a) I-3; (b) C-100, the bright images show the same film at a higher magnification; (c) cross-sectional SEM image of I-3.

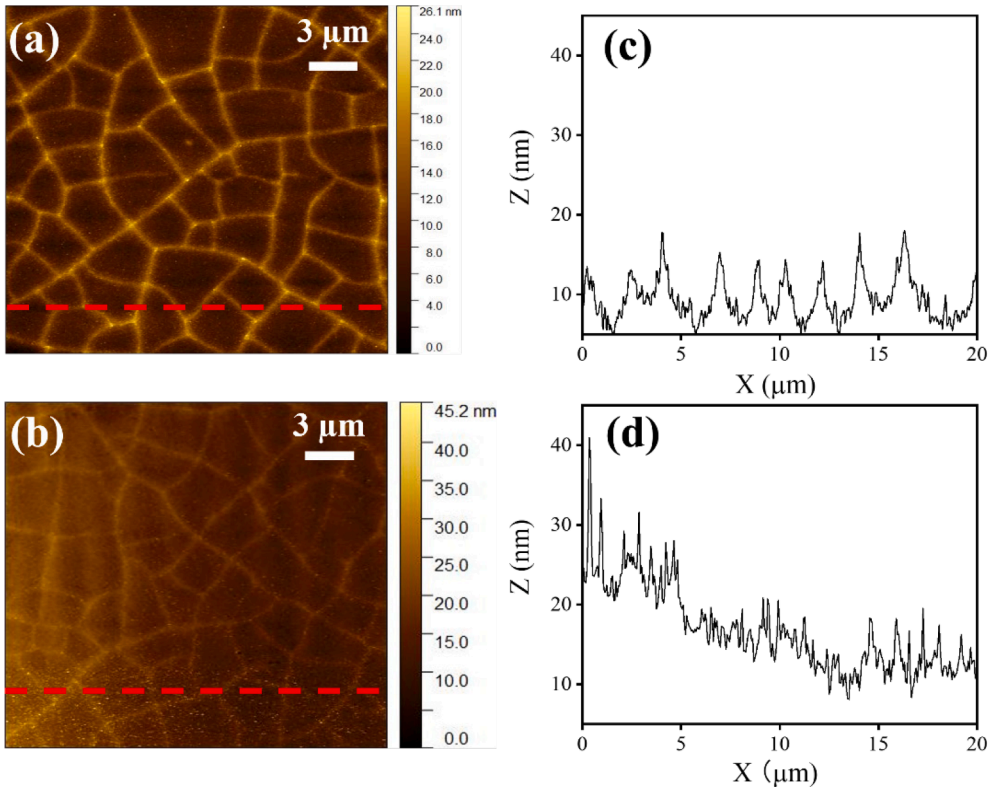


**Fig. 7.** (a and b) AFM images of (a) I-3; (b) C-100; (c and d) Surface profiles along the dashed lines of (c) I-3; (d) C-100.

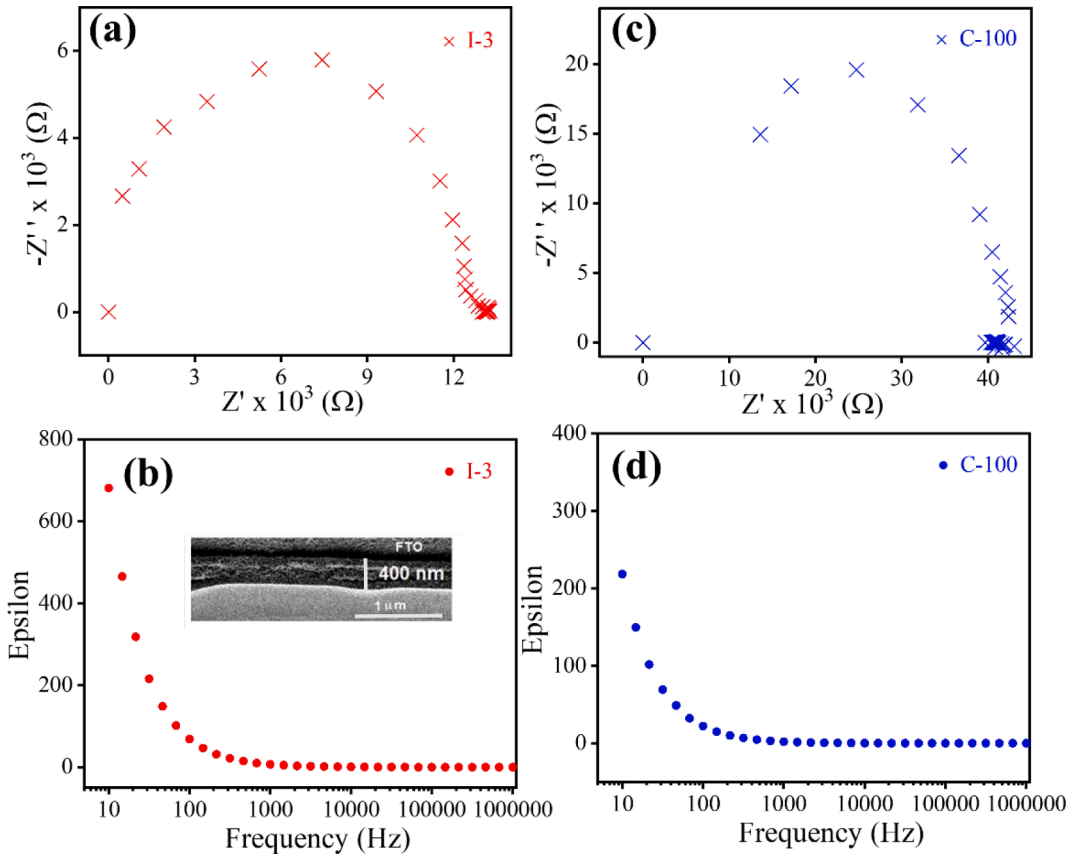


**Fig. 8.** (a and c) Nyquist plots and (c and d) dielectric constant as a function of frequency of I-3 film (a and b) and C-100 (c and d). The insert shows a typical cross-sectional SEM image of I-3 on FTO.

the C-70 film, none of the four bands assigned to tetragonal BTO are observed. Instead, a strong band at 1064 $cm^{-1}$ is detected, corresponding to $BaCO_3$ and aligning with the XRD data [35]. Other bands at 290, 329, 529 and 732 $cm^{-1}$ are observed, which are right shifted peaks of tetragonal BTO (Table 3).

Fig. 5 demonstrates the FTIR spectra of the synthesized films. Both I-3 and C-100 films exhibit an absorption band at 495 $cm^{-1}$ attributed to the normal vibration of the Ti-O bond. Additionally, a weak peak at 1470 $cm^{-1}$, corresponding to crystalline BTO, is also observed in the FTIR spectra of these two samples [36–38]. The FTIR spectrum of C-70 lacks peaks at either 495 or 1470 $cm^{-1}$, while a significant absorption at 1380 $cm^{-1}$, assigned to the symmetric stretching mode of interlayer $CO_3^{2-}$, is observed [39]. Overall, FT-IR spectra provide additional evidence for the presence of crystalline BTO in both I-3 and C-100.

### 3.3. Morphology

Further characterization was performed with SEM over I-3 and C-100 samples as they did not contain impurities of other phases (Fig. 6). Good surface quality, small surface roughness and good homogeneity of the film are evident in the SEM micrograph. It can also be seen that the films are highly agglomerated and noticeable cracks are observed. The depth of cracks is more pronounced in I-3 compared to C-100 while the surface of I-3 is smoother than that of C-100. This observation is consistent with the AFM measurement shown in Fig. 7: a larger number of cracks is visible in I-3 film while which also exhibits a lower surface roughness. The fast calcination step appears to enhance the surface bonding of the film. However, due to the substantial difference in coefficients of thermal expansion (CTE) between the quartz substrate and the film, residual stress within the material leads to cracks formation. The crystal size measured from FE-SEM results aligns well with the average crystallite size in Table 1 which calculated by the Scherrer equation. The surface roughness of I-3 is 12 nm (Fig. 7(c)) while that of C-100 is 36 nm (Fig. 7 (d)). The small particles seen in Fig. 7(c) are agglomerated BTO crystals. The crystals have a spherical shape with a narrow size distribution. The film thickness is approximately 30 crystal layers (400 nm).

The calcination process of C-100 sample was far longer than I-3. Higher temperature or longer calcination time leads to the irregularly shaped crystallite agglomerates of BTO and further leads to less homogeneity and higher surface roughness.

### 3.4. Dielectric constant

Fig. 8(a) and (c) show the Nyquist plots of I-3 and C-100 thin films. The thickness of the BTO thin films deposited between the two electrodes was 400 nm. Fig. 8(b) and (d) show the variation of dielectric constant with frequency ranging from 10 Hz to 1 MHz. A rather high value of dielectric constant in the film obtained under fast heating can be explained by the grain growth during the calcination step [40,41]. This conclusion is also supported by the XRD crystallinity data. It is known that in the sol–gel process, the films are usually dried at some elevated temperature in order to drive out the organic solvents from the gel layer. However, if this process occurs at slow heating or at a constant temperature (typically 300–400 °C), the films are amorphous in nature with very little grain growth. Therefore, it requires a lengthy final sintering process which determines the crystallization into desired phase. But, when the films are immediately heated to high temperature, there is a significant extent of initial grain growth and much higher degree of densification of the gel. Such films, after final sintering, show higher value of dielectric constant than that obtained at slow heating. The dielectric constant values are sharply decreased as frequency increases due to the reduction of space charge polarization effect. The increase of

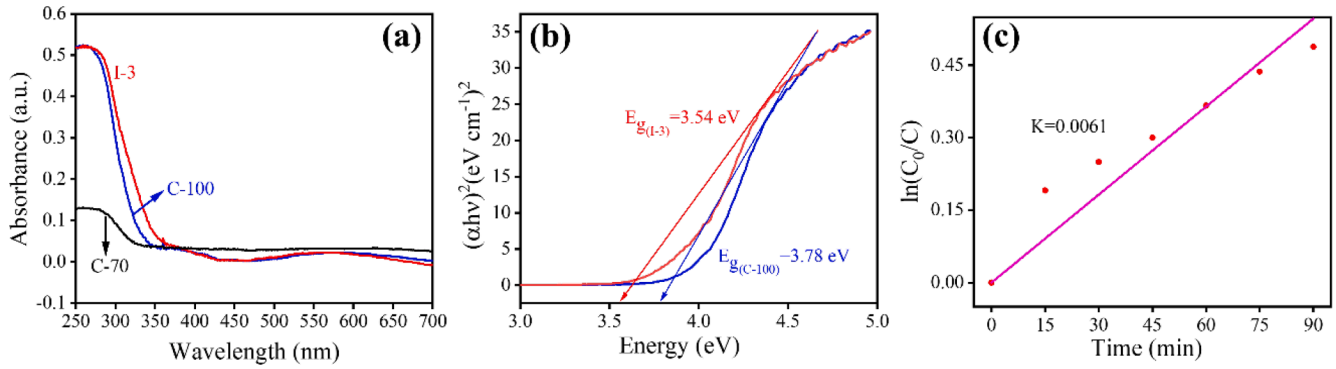


**Fig. 9.** (a) UV–Vis spectra of I-3, C-70 and C-100; (b) Tauc plots of I-3 and C-100; (c) Concentration vs time for methylene blue decomposition over I-3 film. (For interpretation of the references to colour in this figure legend, the reader is referred to the web version of this article.)

dielectric constant in the low frequency range with decreasing grain size can be attributed to the presence of an internal stress in the I-3 sample as confirmed by increased unit cell parameters and tetragonality. Generally, the grain size dependence of the dielectric constant shows consistent trends despite the use of different processing and sintering methods.

### 3.5. Photocatalytic activity

UV–Vis spectra of I-3, C-70 and C-100 films are shown in Fig. 9(a). The absorption patterns are consistent with those previously reported with the strongest absorption occurring at 280 nm [8,36,42–44]. Notably, the absorption intensity of the I-3 and C-100 films is considerably higher compared to that C-70. The semiconductor band gap in the I-3 and C-100 films was 3.54 and 3.78 eV (Fig. 9(b)), respectively. It is clear that the fast-heating method reduces the band gap. The ptotocatalytic kinetics of methylene blue decompositioin under illuminatinon with UV LED light follows a pseudofirst order dependence (Fig. 9(c)). The room temperature kinetic constant of 0.0061 min$^{-1}$ is similar to that reported in other studies with a similar level of catalyst loading.

## 4. Conclusions

Sol-gel derived nanostructured $BaTiO_3$ films were fast-sintered at a heating rate of 540 K min$^{-1}$ for 3 min, and their microstructures and dielectric properties were compared with conventionally sintered samples (with a heating rate of 10 K min$^{-1}$. Fast heating is effective in fabricating highly crystalline tetragonal $BaTiO_3$ thin films, substantially reducing the processing time. The dielectric constant value of the film is 685 at 10 Hz. The film demonstrated a photocatalytic activity in decomposition of methylene blue similar to other semiconductor materials.

## CRediT authorship contribution statement

**Yang Liu:** Writing – original draft, Methodology, Investigation, Formal analysis, Data curation. **Sirui Li:** Supervision, Methodology. **Fausto Gallucci:** Writing – review & editing, Supervision. **Evgeny V. Rebrov:** Writing – review & editing, Supervision, Resources, Funding acquisition, Formal analysis, Data curation, Conceptualization.

## Declaration of competing interest

The authors declare that they have no known competing financial interests or personal relationships that could have appeared to influence the work reported in this paper.

## Data availability

Data will be made available on request.

## Acknowledgements

The authors acknowledge the support from the ERC Grant Surface-Confined fast-modulated Plasma for process and Energy intensification (SCOPE) from the European Commission with grant number 810182. We thank Mrs Ingeborg Schreur for SEM measurements. We also thank Paul Vermeulen, Sidhanth Kanth and Naveen Guruprasad from TU Eindhoven for dielectric constant measurements. Yang Liu thanks Emiel Hessen, Erwin Zoethout and Michael Gleeson for useful discussions. Yang Liu thanks Marco Hendrix, Hao Zhang, Brahim Mezari and Joost Tol for providing equipment training sessions. Yang Liu appreciates support from her parents.

## References

[1] P. Ren, H. Fan, X. Wang, J. Shi, Effects of silver addition on microstructure and electrical properties of barium titanate ceramics, J. Alloys Compd. 509 (2011) 6423–6426, https://doi.org/10.1016/j.jallcom.2011.03.077.
[2] H. Hatono, T. Ito, A. Matsumura, Application of $BaTiO_3$ film deposited by aerosol deposition to decoupling capacitor, Jpn. J. Appl. Phys. 46 (2007) 6915–6919, https://doi.org/10.1143/JJAP.46.6915.
[3] S. Pal, S. Muthukrishnan, B. Sadhukhan, N.V. Sarath, D. Murali, P. Murugavel, Bulk photovoltaic effect in $BaTiO_3$-based ferroelectric oxides: an experimental and theoretical study, J. Appl. Phys. 129 (2021) 084106, https://doi.org/10.1063/5.0036488.
[4] M. Fakhar-e-Alam, S. Saddique, N. Hossain, A. Shahzad, I. Ullah, A. Sohail, M. Khan, M. Saadullah, Synthesis, characterization, and application of $BaTiO_3$ nanoparticles for anti-cancer activity, J. Clust. Sci. 34 (2022) 1745–1755, https://doi.org/10.1007/s10876-022-02346-y.
[5] W. Li, D. Zhou, R. Xu, D. Wang, J. Su, L. Pang, W. Liu, G. Chen, $BaTiO_3$-based multilayers with outstanding energy storage performance for high temperature capacitor applications, ACS Appl. Energy Mater. 8 (2019) 3–10, https://doi.org/10.1021/acsaem.9b00664.
[6] S. Xu, J.C. Whitehead, P.A. Martin, $CO_2$ conversion in a non-thermal, barium titanate packed bed plasma reactor: the effect of dilution by Ar and $N_2$, Chem. Eng. J. 327 (2017) 764–773, https://doi.org/10.1016/j.cej.2017.06.090.
[7] R.S. Abiev, D.A. Sladkovskiy, K.V. Semikin, D.Y. Murzin, E.V. Rebrov, Non-thermal plasma for process and energy intensification in dry reforming of methane, Catalysts 10 (2020) 1358, https://doi.org/10.3390/catal10111358.
[8] S. Kappadan, T. Woldu, S. Thomas, N. Kalarikkal, Materials science in semiconductor processing tetragonal $BaTiO_3$ nanoparticles: an efficient photocatalyst for the degradation of organic pollutants, Mater. Sci. Semicond. Process 51 (2016) 42–47, https://doi.org/10.1016/j.mssp.2016.04.019.
[9] Z. Zhao, D. Wang, R. Gao, G. Wen, M. Feng, G. Song, J. Zhu, D. Luo, H. Tan, X. Ge, W. Zhang, Y. Zhang, L. Zheng, H. Li, Z. Chen, Magnetic-field-stimulated efficient photocatalytic $N_2$ fixation over defective $BaTiO_3$ perovskites, Angew. Chem. Int. Ed. 60 (2021) 11910–11918, https://doi.org/10.1002/anie.202100726.
[10] R. Bel-hadj-tahar, M. Abboud, Structural development and kinetic analysis of $PbTiO_3$ powders processed at low-temperature via new sol-gel approach, Solid State Sci. 78 (2018) 74–85, https://doi.org/10.1016/j.solidstatesciences.2018.02.002.
[11] J. Niu, J. Shi, K. Ouyang, X. Wang, Z. Xu, X. Yu, Microwave-assisted construction of $AgIO_3$ / $BaTiO_3$ heterostructure with excellent photocatalytic activity for tetracycline and methyl blue degradation, J. Alloys Compd. 970 (2024) 172627, https://doi.org/10.1016/j.jallcom.2023.172627.
[12] Y. Yamada, M. Matsubara, A. Muramatsu, S. Takeda, K. Kanie, Highly concentrated solvothermal synthesis of sub-10-nm $BaTiO_3$ nanoparticles for optical applications, Adv. Powder Technol. 33 (2022) 103660, https://doi.org/10.1016/j.apt.2022.103660.

[13] X. Zhang, J. Yue, Y. Zhao, Z. Yan, G. Zhu, L. Liu, Synthesis of tetragonal $BaTiO_3$ nano-particle via a novel tartaric acid co-precipitation process, Ceram. Int. 47 (2021) 7263–7267, https://doi.org/10.1016/j.ceramint.2020.11.006.
[14] R. Ashiri, A. Nemati, M.S. Ghamsari, Crack-free nanostructured $BaTiO_3$ thin films prepared by sol–gel dip-coating technique, Ceram. Int. 40 (2014) 8613–8619, https://doi.org/10.1016/j.ceramint.2014.01.078.
[15] E.S. Reddy, S. Sukumaran, K.C.J. Raju, Microwave assisted synthesis and sintering of lead-free ferroelectric, Mater. Today Proc. 3 (2016) 2213–2219, https://doi.org/10.1016/j.matpr.2016.04.128.
[16] S. Farhadi, S. Sepahvand, Microwave-assisted solid-state decomposition of $La[Co(CN)_6] \cdot 5H_2O$ precursor: a simple and fast route for the synthesis of single-phase perovskite-type $LaCoO_3$ nanoparticles, J. Alloys Compd. 489 (2010) 586–591, https://doi.org/10.1016/j.jallcom.2009.09.117.
[17] C. Fu, W. Cai, L. Zhou, H. Chen, Z. Liu, Synthesis of self-assembly $BaTiO_3$ nanowire by sol–gel and microwave method, Appl. Surf. Sci. 255 (2009) 9444–9446, https://doi.org/10.1016/j.apsusc.2009.07.066.
[18] Y. Yoo, G. Seo, J. Park, J. Kim, J. Jang, Low-temperature rapid UV sintering of sputtered $TiO_2$ for flexible perovskite solar modules, J. Mater. Chem. A 12 (2024) 1562–1572, https://doi.org/10.1039/d3ta05666j.
[19] L. Imhoff, M.B. Di Marco, S.A. Barolin, M.A. Rengifo, M.H. Aguirre, M.G. Stachiotti, Sol–gel synthesis and multiferroic properties of pyrochlore-free Pb $(Fe_{0.5}Nb_{0.5})O_3$ thin films, Ceram. Int. 50 (2024) 5746–5754, https://doi.org/10.1016/j.ceramint.2023.11.361.
[20] W. Zhu, C.C. Wang, S.A. Akbar, R. Asiaie, Fast-sintering of hydrothermally synthesized $BaTiO_3$ powders and their dielectric properties, J. Mater. Sci. 32 (1997) 4303–4307, https://doi.org/10.1023/A:1018663621241.
[21] Y. Zhang, X. Zhao, J. Chen, S. Li, W. Yang, X. Fang, Self-polarized $BaTiO_3$ for greatly enhanced performance of ZnO UV photodetector by regulating the distribution of electron concentration, Adv. Funct. Mater. 30 (2020) 1907650, https://doi.org/10.1002/adfm.201907650.
[22] T.S. Glazneva, E.V. Rebrov, J.C. Schouten, E.A. Paukshtis, Z.R. Ismagilov, Synthesis and characterization of mesoporous silica thin films as a catalyst support on a titanium substrate, Thin Solid Films 515 (2007) 6391–6394, https://doi.org/10.1016/j.tsf.2006.11.058.
[23] F. Ahmad, A. Maqsood, Low-dimensional systems and nanostructures complex impedance, dielectric constant, electric modulus, and conductivity analysis of Cd doped ZnO nanostructures at high temperatures, Phys. E 143 (2022) 115353, https://doi.org/10.1016/j.physe.2022.115353.
[24] A. Tabib, N. Sdiri, H. Elhouichet, M. Férid, Investigations on electrical conductivity and dielectric properties of Na doped ZnO synthesized from sol gel method, J. Alloys Compd. 622 (2015) 687–694, https://doi.org/10.1016/j.jallcom.2014.10.092.
[25] K. Hari, S. Subramanian, T.N. Sairam, G. Amarendra, E.S. Srinadhu, N. Satyanarayana, Structural, electrical and dielectric properties of nanocrystalline $LiMgBO_3$ particles synthesized by Pechini process, J. Alloys Compd. 718 (2017) 459–470, https://doi.org/10.1016/j.jallcom.2017.05.157.
[26] C. Kyu, J. Hoon, D. Yeol, Y. Kim, S. Kim, C. Baek, G. Lee, M. Lee, J. Park, K. Park, Piezoelectric energy conversion by lead-free perovskite $BaTiO_3$ nanotube arrays fabricated using electrochemical anodization, Appl. Surf. Sci. 512 (2020) 144784, https://doi.org/10.1016/j.apsusc.2019.144784.
[27] H. You, S. Li, Y. Fan, X. Guo, Z. Lin, R. Ding, X. Cheng, H. Zhang, T. Woon, B. Lo, J. Hao, Y. Zhu, H. Tam, D. Lei, C. Lam, H. Huang, Accelerated pyro-catalytic hydrogen production enabled by plasmonic local heating of Au on pyroelectric $BaTiO_3$ nanoparticles, Nat. Commun. 13 (2022) 6144, https://doi.org/10.1038/s41467-022-33818-4.
[28] Y. Zhang, Z. Wang, Y. Chen, Z. Zhang, Crystallization kinetics of $PbTiO_3$ ferroelectric films: comparison of microwave irradiation with conventional heating, J. Eur. Ceram. Soc. 38 (2018) 105–111, https://doi.org/10.1016/j.jeurceramsoc.2017.08.030.
[29] W. Cho, E. Hamada, Synthesis of ultrafine $BaTiO_3$ particles from polymeric precursor: their structure and surface property, J. Alloys Compd. 266 (1998) 118–122, https://doi.org/10.1016/S0925-8388(97)00446-5.
[30] P.S. Dobal, A. Dixit, R.S. Katiyar, Z. Yu, R. Guo, A.S. Bhalla, Micro-Raman scattering and dielectric investigations of phase transition behavior in the $BaTiO_3$–$BaZrO_3$ system, J. Appl. Phys. 89 (2001) 8085–8091, https://doi.org/10.1063/1.1369399.
[31] H. Hayashi, T. Nakamura, T. Ebina, In-situ Raman spectroscopy of $BaTiO_3$ particles for tetragonal–cubic transformation, J. Phys. Chem. Solids 74 (2013) 957–962, https://doi.org/10.1016/j.jpcs.2013.02.010.
[32] W. Cho, Structural evolution and characterization od $BaTiO_3$ nanoparticles synthesized from polymeric presursor, J. Phys. Chem. Solids 59 (1998) 659–666, https://doi.org/10.1016/S0022-3697(97)00227-8.
[33] M. DiDomenico, S.H. Wemple, S.P.S. Porto, R.P. Buman, Raman spectrum of single-domain $BaTiO_3$, Phys Rev. 174 (1968) 522–530, https://doi.org/10.1063/1.1369399.
[34] A. Pinczuk, W. Taylor, E. Burstein, The Raman spectrum of $BaTiO_3$, Solid State Commun. 5 (1967) 429–433, https://doi.org/10.1016/0038-1098(67)90791-0.
[35] P. Pasierb, S. Komornicki, M. Rokita, M. Re, Structural properties of $Li_2CO_3 \pm BaCO_3$ system derived from IR and Raman spectroscopy, J. Mol. Struct. 596 (2001) 151–156, https://doi.org/10.1016/S0022-2860(01)00703-7.
[36] M. Rastogi, H.S. Kushwaha, R. Vaish, Highly efficient visible light mediated azo dye degradation through barium titanate decorated reduced graphene oxide sheets, Electron. Mater. Lett. 12 (2016) 281–289, https://doi.org/10.1007/s13391-015-5274-8.
[37] Y.S.A. Selmi, E.H.M.A. Almessiere, A.B.I. Ercan, Impact of ZnO addition on structural, morphological, optical, dielectric and electrical performances of $BaTiO_3$ ceramics, J. Mater. Sci. Mater. Electron. 30 (2019) 9520–9530, https://doi.org/10.1007/s10854-019-01284-2.
[38] Y. Ni, H. Zheng, N. Xiang, K. Yuan, J. Hong, Simple hydrothermal synthesis and photocatalytic performance of coral-like $BaTiO_3$ nanostructures, RSC Adv. 5 (2015) 7245–7252, https://doi.org/10.1039/c4ra13642j.
[39] E. Alibakhshi, E. Ghasemi, M. Mahdavian, B. Ramezanzadeh, Corrosion inhibitor release from Zn-Al-$[PO_4^{3-}]$-$[CO_3^{2-}]$ layered double hydroxide nanoparticles, Prog. Color Colorants Coat. 9 (2016) 233–248, https://doi.org/10.30509/PCCC.2016.75889.
[40] W. Maison, R. Kleeberg, R.B. Heimann, S. Phanichphant, Phase content, tetragonality, and crystallite size of nanoscaled barium titanate synthesized by the catecholate process: effect of calcination temperature, J. Eur. Ceram. Soc. 23 (2003) 127–132, https://doi.org/10.1016/S0955-2219(02)00071-7.
[41] H. Pawar, M. Khan, M. Kumari, U.K.D. Tara, P. Ranveer, Role of calcination on dielectric properties of $BaTiO_3$ nanoparticles as a gas sensor, Appl. Phys. A 127 (2021) 1–10, https://doi.org/10.1007/s00339-021-04517-6.
[42] P. Claverie, S. Sun, I.C. Amaechi, A.H. Youssef, D. Rawach, A. Ruediger, Ferroelectric Fe−Cr codoped $BaTiO_3$ nanoparticles for the photocatalytic oxidation of Azo dyes, ACS Appl. Nano Mater. 2 (2019) 2890–2901, https://doi.org/10.1021/acsanm.9b00336.
[43] S. Ramakanth, K.C. James Raju, Band gap narrowing in $BaTiO_3$ nanoparticles facilitated by multiple mechanisms, J. Appl. Phys. 115 (2014) 173507, https://doi.org/10.1063/1.4871776.
[44] A.U.L.S. Setyadi, F. Nurosyid, Y. Iriani, Influence of holding time annealing process on the microstructure and optical properties of barium titanate ($BaTiO_3$) thin film using the sol-gel method, AIP Conf. Proc. 2202 (2019) 020034, https://doi.org/10.1063/1.5141647.